Article

# Non-volatile electric control of spin–charge conversion in a $SrTiO_3$ Rashba system

https://doi.org/10.1038/s41586-020-2197-9

Received: 20 August 2019

Accepted: 25 February 2020

Published online: 22 April 2020

Check for updates

Paul Noël[1,4,6], Felix Trier[2,6], Luis M. Vicente Arche[2], Julien Bréhin[2], Diogo C. Vaz[2,5], Vincent Garcia[2], Stéphane Fusil[2,3], Agnès Barthélémy[2], Laurent Vila[1], Manuel Bibes[2]✉ & Jean-Philippe Attané[1]✉

After 50 years of development, the technology of today's electronics is approaching its physical limits, with feature sizes smaller than 10 nanometres. It is also becoming clear that the ever-increasing power consumption of information and communication systems[1] needs to be contained. These two factors require the introduction of non-traditional materials and state variables. As recently highlighted[2], the remanence associated with collective switching in ferroic systems is an appealing way to reduce power consumption. A promising approach is spintronics, which relies on ferromagnets to provide non-volatility and to generate and detect spin currents[3]. However, magnetization reversal by spin transfer torques[4] is a power-consuming process. This is driving research on multiferroics to achieve low-power electric-field control of magnetization[5], but practical materials are scarce and magnetoelectric switching remains difficult to control. Here we demonstrate an alternative strategy to achieve low-power spin detection, in a non-magnetic system. We harness the electric-field-induced ferroelectric-like state of strontium titanate ($SrTiO_3$)[6–9] to manipulate the spin–orbit properties[10] of a two-dimensional electron gas[11], and efficiently convert spin currents into positive or negative charge currents, depending on the polarization direction. This non-volatile effect opens the way to the electric-field control of spin currents and to ultralow-power spintronics, in which non-volatility would be provided by ferroelectricity rather than by ferromagnetism.

'Spin–orbitronics'[12] exploits the interplay between charge currents and spin currents enabled by spin–orbit coupling (SOC) in non-magnetic systems. It allows the generation of pure spin currents from charge currents and vice versa, without resorting to ferromagnetic materials. The Edelstein effect[13] allows charge–spin conversion[14] with an efficiency comparable to or larger than that of the spin Hall effect[15]. It typically occurs at Rashba surfaces and interfaces[16] where inversion symmetry breaking results in an out-of-plane electric field. In the presence of SOC, this leads to a locking of the momentum and spin degrees of freedom. The flow of an in-plane charge current in such a system produces a transverse spin density, which can diffuse as a spin current in an adjacent material[13]. Conversely, injecting a spin density results in the production of a net charge current by the inverse Edelstein effect[17]. As such, Rashba systems can be used as spin generators and detectors. However, the conversion rate is inherently set by the electronic structure, and cannot be switched by an external stimulus.

The order parameter of ferroelectrics (polarization) can be switched by an electric field for energy costs typically 1,000 times smaller[2] than those for switching ferromagnets. Moreover, ferroelectrics can harbour intense electric fields, substantially modifying the carrier densities in adjacent materials, and thereby tuning their properties in a non-volatile fashion. An exciting route towards low-power electronics would thus be to combine the remanence of ferroelectrics with the ability to generate and manipulate spin currents by the direct and inverse Edelstein effects in Rashba systems. Beyond magnetoelectricity, ferroelectric Rashba architectures would therefore offer a new approach to the non-volatile control of spin currents by electric fields, with ultralow-power operation.

Most efforts to identify single-phase Rashba ferroelectrics[18] have focused on GeTe (ref. [19]). However, ferroelectric properties are poor[20] because of high leakage, and spin–charge conversion experiments have yielded a moderate efficiency[21]. Here we show that beyond bulk materials, interface systems combining Rashba SOC and a switchable polarization enable the non-volatile electric control of a highly efficient spin–charge conversion.

The general concept of ferroelectricity-controlled spin–charge conversion is described in Fig. 1. At the interface between a ferroelectric and an ultrathin SOC system—such as a heavy metal, a Weyl semi-metal, or a two-dimensional electron gas (2DEG)—electrons are accumulated or depleted depending on the polarization direction (Fig. 1a). This modifies the electric field in the interface region, and in the ideal case changes its sign. If a Rashba state is present in the SOC system at the interface with the ferroelectric, reversing the sign of the local electric field reverses the chirality of the spin textures in both split

[1]Université Grenoble Alpes, CEA, CNRS, Spintec, Grenoble, France. [2]Unité Mixte de Physique, CNRS, Thales, Université Paris-Saclay, Palaiseau, France. [3]Université d'Evry, Université Paris-Saclay, Evry, France. [4]Present address: ETH Zürich, Zurich, Switzerland. [5]Present address: CIC Nanogune, Donostia–San Sebastian, Spain. [6]These authors contributed equally: Paul Noël, Felix Trier. ✉e-mail: manuel.bibes@cnrs-thales.fr; jean-philippe.attane@cea.fr

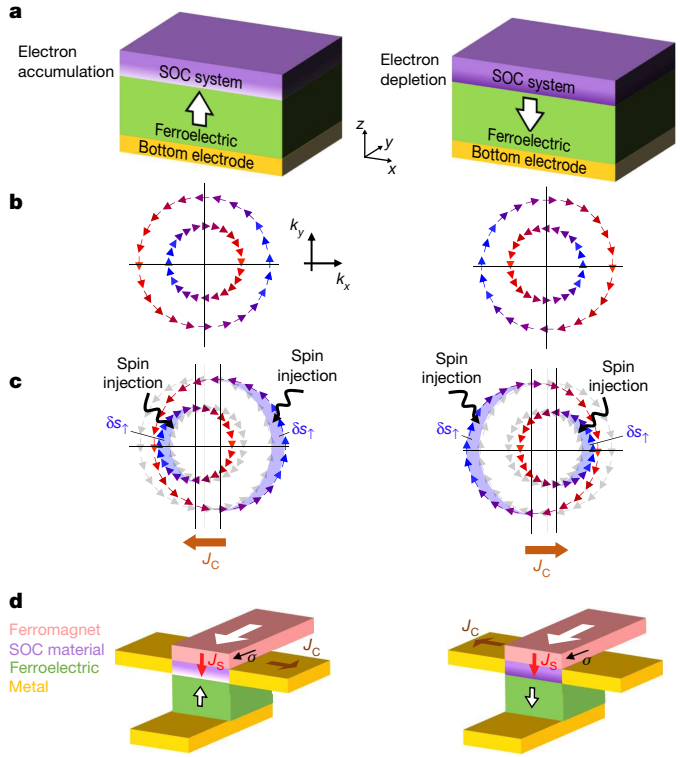


**Fig. 1 | Concept of ferroelectricity-controlled spin–charge conversion.** **a**, Sketch of a ferroelectric Rashba architecture combining a ferroelectric material (green) and a material with spin–orbit coupling (SOC; purple). Upon switching polarization, electrons are accumulated (left) or depleted (right) in the SOC material (for example, a 2DEG), creating an electric field whose sign depends on the polarization direction. **b**, Corresponding Rashba-split chiral Fermi contours with spin-momentum locking. The chirality of the contours switches upon switching the ferroelectric polarization. $k_x$ and $k_y$ correspond to the $x$ and $y$ axes in momentum space. Blue and red colours indicate the spin direction (blue, along $k_y$; red, along $-k_y$). **c**, Inverse Edelstein effect in a Rashba interface. When a spin current is injected (for example, by spin pumping) with a spin polarization along the $y$ axis, the spin population is altered, causing a displacement of the two inequivalent Fermi surfaces (red and blue lines) by $\pm\Delta k$ in momentum space. This results in a net charge current generated perpendicularly to the spin current and to its spin polarization. The sign of the generated current depends on the chirality of the Fermi contours and is thus reversed upon switching ferroelectric polarization. $\delta s_\uparrow$ corresponds to the injected excess of spin-up density. **d**, Non-volatile device operated by ferroelectricity and Rashba SOC. Through the inverse Edelstein effect a charge current $J_C$ is generated by the conversion of a spin current $J_S$ injected from the ferromagnet. The sign of $J_C$ changes with the direction of the ferroelectric polarization. The large white arrows show the ferromagnet magnetization, the small black arrows the spin $\sigma$, the brown arrows the direction of the charge current $J_C$, and the red arrow the direction of the spin current $J_S$. The small black-and-white arrows correspond to the ferroelectric polarization.

Fermi contours (Fig. 1b). Through the inverse Edelstein effect[13], the injection of a spin current into the Rashba state will produce a charge current $J_C$ whose sign will depend on the ferroelectric polarization state (Fig. 1c). This mechanism offers the possibility to design a wealth of devices such as the bipolar memory proposed in Fig. 1. It can also be the basis of logic devices[22] akin to the magnetoelectric spin–orbit (MESO) device proposed by Intel[23], but without resorting to a multiferroic to switch the ferromagnet.

To experimentally demonstrate the non-volatile electric control of the spin–charge conversion, we use $SrTiO_3$ (STO) 2DEGs, generated by the deposition of a film of Al onto a STO single crystal[24,25]. Indeed, STO 2DEGs exhibit a sizeable Rashba SOC[10] with a very high conversion efficiency[25,26]. In addition, STO is a quantum paraelectric that develops an electric-field-induced switchable polarization at low temperature[7–9].

The spin-to-charge conversion was measured by using spin pumping by ferromagnetic resonance on a NiFe(20 nm)/Al(0.9 nm)//STO sample (see Fig. 2a inset). The nominally 500-μm-thick STO substrate was thinned down to 250 ± 20 μm using mechanical polishing, allowing the application of high electric fields ($E$). A static magnetic field was applied along the $y$ direction. At the ferromagnetic resonance, a pure spin current is injected into the 2DEG along the $-z$ direction, with spins oriented along $y$ (ref. [27]). The measurement of the extra damping due to this relaxation channel allows calculation of the injected spin current[26,27]. In the 2DEG, this spin current is then converted into a charge current oriented along $x$ by the inverse Edelstein effect. Since the sample is in open circuit, at the resonance field this results in a voltage drop along the sample, in the $x$ direction[26].

In the pristine, ungated state, the voltage drop obtained at resonance corresponds to the production of a positive normalized current of 1.2 A $mT^{-2}$ $m^{-1}$ (top left panel of Fig. 2b). At low temperature, STO is known to undergo a phase transition at high electric field[7–9]: once a large electric field has been applied, the material develops a switchable, remanent polarization. This phenomenon is often referred to as a field-induced ferroelectric order or a field-induced ferroelectric-like state. We applied voltages up to ±200 V, corresponding to $E$ up to ±8 kV $cm^{-1}$, high enough to achieve this phase transition[7,9]. After a first initialization cycle [+200 V; −200 V; +200 V], the gate-voltage dependence of the spin-pumping signal shows a hysteretic behaviour (Fig. 2a). The charge currents produced at ferromagnetic resonance have opposite signs for +200 V and −200 V gate voltages, as seen in points B, F and D of Fig. 2a and b. After applying the maximum voltage, the normalized current reaches a very high amplitude (±8.8 A $mT^{-2}$ $m^{-1}$), beyond the record values obtained previously in $LaAlO_3$/STO and Al/STO samples (around 5 A $mT^{-2}$ $m^{-1}$)[26]. The spin–charge conversion efficiency is quantified by the inverse Edelstein length $\lambda_{IEE}$, equal to the ratio of the 2D charge current density produced by the injected 3D spin current, that is, $\lambda_{IEE} = J_C^{2D}/J_S^{3D}$ (ref. [17]; see Methods). Here we estimate $\lambda_{IEE} \approx \pm 60$ nm, a value one to two orders of magnitude larger than in metallic Rashba interfaces[17] or topological insulators[28].

We note that the produced current—and thus the spin–charge conversion rate—is remanent at gate voltage $V_{gate} = 0$ V, as seen in C and E in Fig. 2a and b. Similar hysteretic behaviours have been obtained on several thinned-down samples but not on a 500-μm-thick STO substrate, which indicates the existence of a critical electric field for the hysteresis to appear. The non-volatile control of the spin–charge conversion is further evidenced by Fig. 2c, which displays the normalized charge current produced at 0 V after the application of 500-ms pulses of ±200 V gate voltage. Figure 2d shows the temperature dependence of the difference $\Delta I_C$ in the produced current obtained at remanence after applying pulses of +200 V and −200 V at 7 K. $\Delta I_C$ is large below 30 K and vanishes above 45–50 K, suggesting a transition of STO into the paraelectric phase[7–9]. Extended Data Figs. 1 and 4 show that the effect is reproducible and stable in time for at least several hours.

We have also performed electric polarization measurements on a Al(1.8 nm)//STO 2DEG sample with a STO thickness of 200 ± 20 μm. As visible in Fig. 3a, the application of an electric field up to 2.5 kV $cm^{-1}$ (green curve) yields a linear dependence of the polarization with $E$, as expected for a dielectric. However, when the voltage exceeds about 7 kV $cm^{-1}$, a hysteresis develops, associated with switching current peaks in the $I$ versus $E$ data (Fig. 3a inset). The saturation polarization is about 4 μC $cm^{-2}$, in agreement with earlier reports[7]. Upon increasing the temperature (Fig. 3c), the loop progressively closes, indicating a Curie temperature close to 50 K (Fig. 3b). This almost coincides with the temperature at which the remanent spin–charge conversion effect vanishes (Fig. 2d), strongly suggesting that the switchable polarization is at the origin of the hysteretic inverse Edelstein effect. At low temperature, reducing $E$ to below the critical value still yields

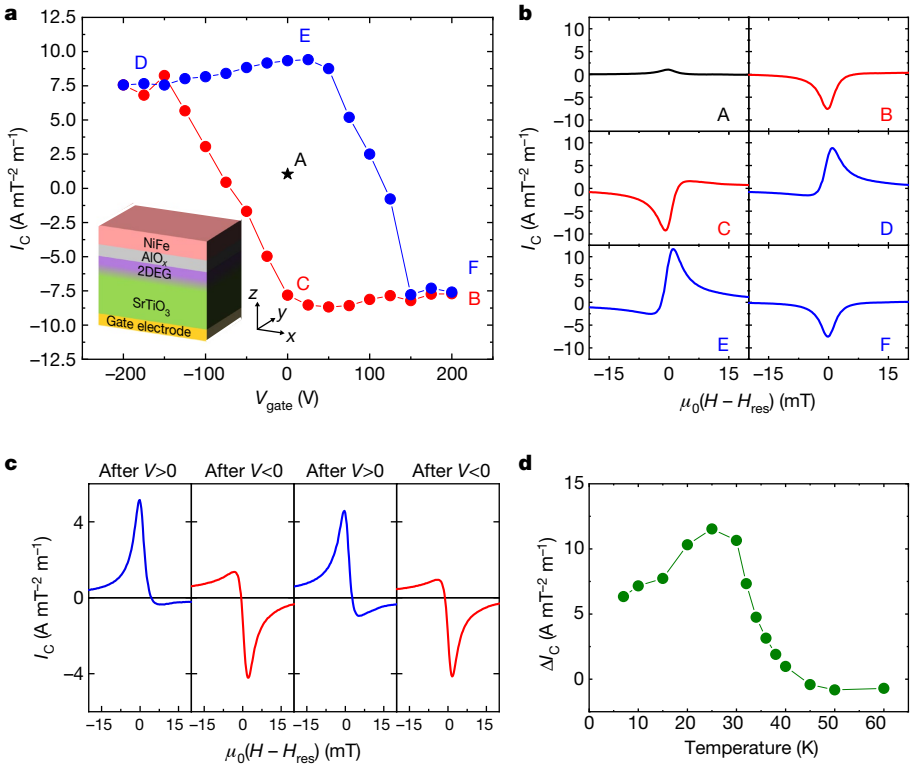


**Fig. 2 | Electric-field-controlled spin–charge conversion with electrical remanence. a**, Gate-voltage dependence of the normalized current produced by the inverse Edelstein effect. A–F, $I_C$ conditions examined in **b**. Inset, a sketch of the heterostructure. **b**, Magnetic-field dependence of the normalized current produced in spin-pumping experiments, for different voltage values (see **a**). **c**, Normalized charge current produced at electrical remanence after applying positive or negative voltage pulses of ±200 V. All data have been measured at 7 K. **d**, Temperature dependence of the difference between the remanent normalized currents after the application of a large positive or negative voltage.

hysteretic polarization loops, albeit with a lower remanent polarization (Fig. 4a).

One of the hallmark features of STO 2DEGs is the strong gate-voltage dependence of the sheet resistance[29] $R_S$. In thick STO samples the gate dependence of $R_S$ is usually non-hysteretic[30], in line with the paraelectric nature of STO at low electric fields. Here, as seen in Fig. 4b, $R_S$ varies as the carrier density varies, but this dependence also exhibits a clear hysteresis, allowing the non-volatile electric control

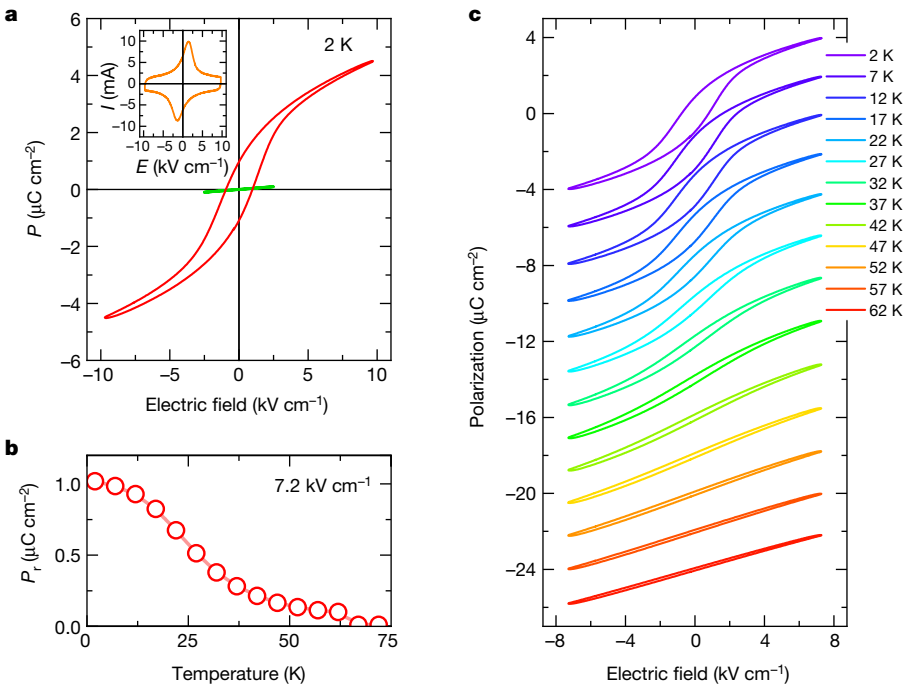


**Fig. 3 | Electric polarization measurements. a**, Polarization versus electric field curves measured on a Al(1.8 nm)//STO sample. The green curve corresponds to the polarization loop measured with a maximum field of 2.5 kV cm$^{-1}$. Inset, corresponding current versus electric field curve. **b**, Temperature dependence of the remanent polarization $P_r$. **c**, Polarization loops at different temperatures.

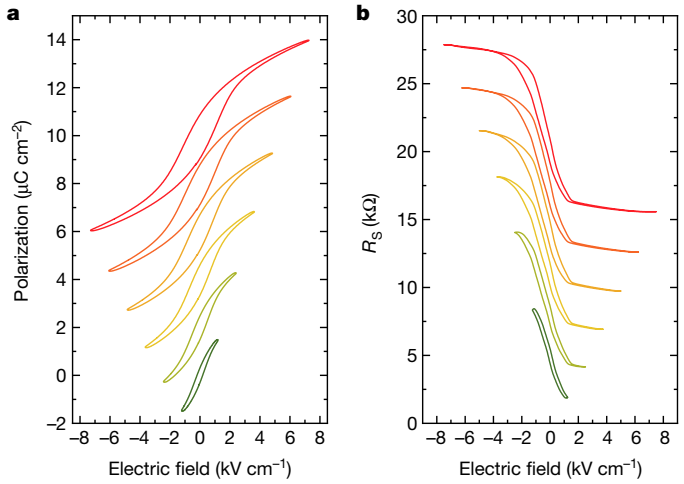


**Fig. 4 | Field effect experiments. a**, Polarization loops at 2 K measured in the field-induced state for different increasing maximum electric fields. The curves are shifted by 2 μC cm$^{-2}$ for clarity. **b**, Gate dependence of the 2DEG sheet resistance $R_S$ for different maximum electric fields at 2 K. The curves are shifted by 3 kΩ for clarity.

of the 2DEG electronic properties. We note that the hysteresis amplitude increases upon increasing the maximum $E$, so that the $R_S$ versus $E$ loops mimic the polarization loops of Fig. 4a. Hall measurements made in the two remanent states yield a difference in carrier densities $\Delta n_s = 5.45 \times 10^{12}$ cm$^{-2}$, only two times smaller than the theoretical value $\Delta n_s = 2P_r/e = 1.13 \times 10^{13}$ cm$^{-2}$ (using the remanent polarization $P_r = 0.9$ μC cm$^{-2}$); this corresponds to a notable efficiency compared to the literature[31,32]. Note that we have also performed $R_S$ versus $E$ loops on spin-pumping samples, which possess a NiFe layer, showing that the obtained loops are very similar to the $\lambda_{IEE}$ versus $V_{gate}$ loops (see Extended Data Fig. 1 and Methods).

Several mechanisms may be invoked to explain our observation of a hysteretic inverse Edelstein effect. One can be related to the description of Fig. 1a, namely, a local inversion of the electric field in the SOC material (here the 2DEG) promoting polarization-direction-dependent Rashba SOC and spin–charge conversion. Additionally, electronic structure effects may be at play, since the multiorbital band structure of STO 2DEGs is known to produce effective Rashba effects with opposite signs, depending on the orbitals involved[25,26]. Moreover, the presence of a switchable polarization with associated polar displacements of cations and anions should substantially modify the band structure compared to the paraelectric case. This may generate additional (avoided) band crossings, possibly with non-trivial topology[25], leading to super-efficient spin–charge conversion.

Our results constitute the basis of a new type of spintronics, in which non-volatility would not originate from ferromagnetism but from ferroelectricity. They could be extended to room temperature by, for example, designing 2DEGs on strained STO thin films[33] or $BaTiO_3$ (ref. [24]). This could open the way to a new class of ultralow-power spin–orbitronic devices (such as memories, spin field-effect transistors, spin Hall transistors or MESO-like logic devices). In the future, demonstration of a non-volatile electric control of the direct Edelstein effect could additionally lead to reconfigurable spin–orbit torque memories and logic gates, be of benefit to the manipulation of skyrmions or domain walls, and allow the development of agile terahertz emitters and spin-wave logic architectures.

## Online content

Any methods, additional references, Nature Research reporting summaries, source data, extended data, supplementary information, acknowledgements, peer review information; details of author contributions and competing interests; and statements of data and code availability are available at [https://doi.org/10.1038/s41586-020-2197-9].


1. Jones, N. How to stop data centres from gobbling up the world's electricity. *Nature* **561**, 163–166 (2018).
2. Manipatruni, S., Nikonov, D. E. & Young, I. A. Beyond CMOS computing with spin and polarization. *Nat. Phys.* **14**, 338–343 (2018).
3. Žutić, I., Fabian, J. & Das Sarma, S. Spintronics: fundamentals and applications. *Rev. Mod. Phys.* **76**, 323–410 (2004).
4. Slonczewski, J. C. Current-driven excitation of magnetic multilayers. *J. Magn. Magn. Mater.* **159**, L1–L7 (1996).
5. Heron, J. T. et al. Deterministic switching of ferromagnetism at room temperature using an electric field. *Nature* **516**, 370–373 (2014).
6. Gränicher, H. Induzierte Ferroelektricität von $SrTiO_3$ bei sehr tiefen Temperaturen und über die Kälteerzeugung durch adiabatische Entpolarisierung. *Helv. Phys. Acta* **29**, 210–212 (1956).
7. Hemberger, J., Lunkenheimer, P., Viana, R., Böhmer, R. & Loidl, A. Electric-field-dependent dielectric constant and nonlinear susceptibility in $SrTiO_3$. *Phys. Rev. B* **52**, 13159–13162 (1995).
8. Sidoruk, J. et al. Quantitative determination of domain distribution in $SrTiO_3$ — competing effects of applied electric field and mechanical stress. *J. Phys. Condens. Matter* **22**, 235903 (2010).
9. Manaka, H., Nozaki, H. & Miura, Y. Microscopic observation of ferroelectric domains in $SrTiO_3$ using birefringence imaging techniques under high electric fields. *J. Phys. Soc. Jpn* **86**, 114702 (2017).
10. Caviglia, A. D. et al. Tunable Rashba spin-orbit interaction at oxide interfaces. *Phys. Rev. Lett.* **104**, 126803 (2010).
11. Ohtomo, A. & Hwang, H. Y. A high-mobility electron gas at the $LaAlO_3/SrTiO_3$ heterointerface. *Nature* **427**, 423–426 (2004); correction 441, 120 (2006).
12. Soumyanarayanan, A., Reyren, N., Fert, A. & Panagopoulos, C. Emergent phenomena induced by spin–orbit coupling at surfaces and interfaces. *Nature* **539**, 509–517 (2016).
13. Edelstein, V. M. Spin polarization of conduction electrons induced by electric current in two-dimensional asymmetric electron systems. *Solid State Commun.* **73**, 233–235 (1990).
14. Kondou, K. et al. Fermi-level-dependent charge-to-spin current conversion by Dirac surface states of topological insulators. *Nat. Phys.* **12**, 1027–1031 (2016).
15. Hoffmann, A. Spin Hall effects in metals. *IEEE Trans. Magn.* **49**, 5172–5193 (2013).
16. Bychkov, Y. A. & Rashba, E. I. Properties of a 2D electron gas with lifted spectral degeneracy. *JETP Lett.* **39**, 78–81 (1984).
17. Sánchez, J. C. R. et al. Spin-to-charge conversion using Rashba coupling at the interface between non-magnetic materials. *Nat. Commun.* **4**, 2944 (2013).
18. Picozzi, S. Ferroelectric Rashba semiconductors as a novel class of multifunctional materials. *Front. Phys.* **2**, https://doi.org/10.3389/fphy.2014.00010 (2014).
19. Rinaldi, C. et al. Ferroelectric control of the spin texture in GeTe. *Nano Lett.* **18**, 2751–2758 (2018).
20. Kolobov, A. V. et al. Ferroelectric switching in epitaxial GeTe films. *APL Mater.* **2**, 066101 (2014).
21. Rinaldi, C. et al. Evidence for spin to charge conversion in GeTe(111). *APL Mater.* **4**, 032501 (2016).
22. Bibes, M., Vila, L., Attané, J.-P., Noël, P. & Vaz, D. C. Dispositif électronique, porte numérique, composant analogique et procédé de génération d'une tension. French patent FR18 74319 (2018).
23. Manipatruni, S. et al. Scalable energy-efficient magnetoelectric spin–orbit logic. *Nature* **565**, 35–42 (2019).
24. Rödel, T. C. et al. Universal fabrication of 2D electron systems in functional oxides. *Adv. Mater.* **28**, 1976–1980 (2016).
25. Vaz, D. C. et al. Mapping spin–charge conversion to the band structure in a topological oxide two-dimensional electron gas. *Nat. Mater.* **18**, 1187–1193 (2019).
26. Lesne, E. et al. Highly efficient and tunable spin-to-charge conversion through Rashba coupling at oxide interfaces. *Nat. Mater.* **15**, 1261–1266 (2016).
27. Tserkovnyak, Y., Brataas, A. & Bauer, G. E. W. Enhanced Gilbert damping in thin ferromagnetic films. *Phys. Rev. Lett.* **88**, 117601 (2002).
28. Noel, P. et al. Highly efficient spin-to-charge current conversion in strained HgTe surface states protected by a HgCdTe layer. *Phys. Rev. Lett.* **120**, 167201 (2018).
29. Caviglia, A. D. et al. Electric field control of the $LaAlO_3/SrTiO_3$ interface ground state. *Nature* **456**, 624–627 (2008).
30. Biscaras, J. et al. Limit of the electrostatic doping in two-dimensional electron gases of $LaXO_3$(X = Al, Ti)/$SrTiO_3$. *Sci. Rep.* **4**, 6788 (2015).
31. Crassous, A. et al. Nanoscale electrostatic manipulation of magnetic flux quanta in ferroelectric/superconductor $BiFeO_3$ / $YBa_2Cu_3O_{7-\delta}$ heterostructures. *Phys. Rev. Lett.* **107**, 247002 (2011).
32. Yamada, H. et al. Ferroelectric control of a Mott insulator. *Sci. Rep.* **3**, 2834 (2013).
33. Haeni, J. H. et al. Room-temperature ferroelectricity in strained $SrTiO_3$. *Nature* **430**, 758–761 (2004).

# Methods

### Sample preparation

NiFe and Al films were deposited at room temperature by d.c. magnetron sputtering on $TiO_2$-terminated (001)-oriented STO substrates (from CrysTec). $TiO_2$-termination was achieved through a chemical treatment, where the substrate was submerged in a buffered hydrofluoric acid ($NH_4F$-HF 7:1) for 30 s and annealed under an oxygen-rich environment at 1,000 °C for 3 h. Before deposition, the STO substrates were additionally annealed at 730 °C for 2 h under a partial oxygen pressure of 400 mbar. The deposition of the metallic layers was performed under an Ar partial pressure of $4.5\times10^{-4}$ mbar and a substrate-to-target distance of 7 cm. The samples including NiFe were additionally capped with a 2.5-nm layer of Al, which becomes oxidized when exposed to air. Samples were mechanically polished on diamond pads under deionized water flow.

### Spin pumping

The spin-pumping experiments were carried out using a Bruker ESP300E X-band CW spectrometer at 9.68 GHz, with a loop-gap Bruker ER 4118X-MS5 cavity, and using a microwave power of 5 mW or less to remain in the linear regime. The generated d.c. voltage was measured using a Keithley 2182A nanovoltmeter. The gate voltage was applied using a Keithley 2400 sourcemeter. The measured signals were observed to be linear with the r.f. power up to 5 mW.

### Calculation of the inverse Edelstein length

The inverse Edelstein length $\lambda_{IEE}$ is the figure of merit quantifying the efficiency of the spin to charge current conversion. It has the dimension of a length, as the 3D spin current $J_S^{3D}$ (in A m$^{-2}$) is converted into a 2D charge current $J_C^{2D}$ (in A m$^{-1}$):

$$\lambda_{IEE}=\frac{J_C^{2D}}{J_S^{3D}} \tag{1}$$

Both $J_S^{3D}$ and $J_C^{2D}$ need to be evaluated to calculate the inverse Edelstein length. Here we use the method already described in previous works (for example, on LAO/STO (ref. [26]) or HgTe (ref. [28])).

The produced charge current is simply extracted from the symmetric component of the measured spin signal $V_{sym}$:

$$J_C^{2D}=\frac{V_{sym}}{Rw} \tag{2}$$

where $R$ is the resistance of the sample (measured independently), and $w$ is the sample width (400 μm).

Note that here, the produced current $J_C^{2D}$ is used to give the amplitude of the spin signal, as it can be considered as raw data. In order to have values comparable from measurement to measurement, especially with experiments found in the literature, and as the spin signal varies linearly with the square of the excitation field $\mu_0 h_{rf}$ ($h_{rf}$ is the radio-frequency field), the current production has to be normalized. Thus, the produced current given in the main text is actually $J_C^{2D}/(\mu_0 h_{rf})^2$, in A mT$^{-2}$ m$^{-1}$. The radiofrequency field for a given measurement is measured using the cavity conversion factor.

The spin current is extracted using the spin-pumping theory first developed by Tserkovnyak, Brataas[27,34] and co-workers, and then by several other groups[35,36]. The spin current injected at the ferromagnetic resonance can be obtained by measuring some of the magnetic properties of the ferromagnetic layer, and by calculating the effective spin mixing conductance:

$$G_{eff}^{\uparrow\downarrow}=\frac{4\pi M_s t_{FM}}{g\mu_B}(\alpha-\alpha_{ref}) \tag{3}$$

where $\mu_B$ is the Bohr magneton, $t_{FM}$ the thickness of the ferromagnetic material (20 nm here), $M_s$ the saturation magnetization of the Permalloy thin film, $g$ its $g$-factor, $\alpha$ its Gilbert damping, and $\alpha_{ref}$ the Gilbert damping of a Permalloy thin film without a spin-sink (here Permalloy on native Si). All these values are extracted from independent ferromagnetic resonance (FMR) measurements, using either broadband-FMR or out-of-plane angular dependence measurements.

Then, using the expression of the spin mixing conductance we can obtain the injected spin current:

$$J_S^{3D}=\frac{G_{eff}^{\uparrow\downarrow}\gamma^2\hbar\mu_0 h_{rf}^2}{8\pi\alpha^2}\left[\frac{4\pi M_s\gamma+\sqrt{(4\pi M_s\gamma)^2+4\omega^2}}{(4\pi M_s\gamma)^2+4\omega^2}\right]\frac{2e}{\hbar} \tag{4}$$

where $\gamma$ is the gyromagnetic ratio, $\omega$ the angular frequency, $e$ the elementary charge and $\hbar$ the reduced Planck constant. The inverse Edelstein length can then be obtained by combining equations (1), (2) and (4).

### Gate-voltage dependence reproducibility

We have performed spin-pumping measurements on different samples of NiFe(20 nm)/Al(0.9 nm)//STO at 7 K, see Extended Data Fig. 1. Sample 1 is taken from a first batch, whereas samples 2 and 3 are two different samples from the same second batch. The results shown in the main text have been measured on sample 3. After thin film deposition on STO substrates, the samples were all thinned down to the same thickness (250 ± 20 μm). As can be seen in Extended Data Fig. 1, for these three samples similar gate-voltage dependences have been obtained, with a hysteretic behaviour, a positive or negative remanent spin-signal at $V_{gate}=0$ V, and large conversion efficiencies. The obtained inverse Edelstein lengths $\lambda_{IEE}$ are above 40 nm in all three cases, and up to 60 nm in the case of sample 3. The error bars are mostly due to the uncertainty on the effective spin mixing conductance. The main results presented in the text are thus reproducible, even though the samples have been thinned down using mechanical polishing.

We have also performed several cool-downs on the same sample. After performing a first cool-down and some gate dependence measurements at low temperature, it is possible to recover the initial state by heating up the sample at room temperature. As can be seen in Extended Data Fig. 2 (measured on sample 2), the remanent ferroelectric state is lost after heating, but when going back to 7 K the sample recovers the initial state, with a lower and positive spin signal. This is consistent with our observation of a voltage-induced ferroelectricity at low temperature. After heating at room temperature, an initialization loop [+200 V; −200 V; +200 V] performed at low temperature allows retrieval of the hysteretic behaviour and the remanence of the polarization.

### Time stability of the remanent state

In the main text we show that a ±200 V gate-voltage application at 7 K allows the spin–charge conversion to be controlled in a remanent way. To demonstrate the non-volatility associated with this remanence, we performed spin-pumping measurements hours after applying a gate voltage of either +200 V or −200 V for 500 ms. As seen in Extended Data Fig. 3, the produced normalized current is preserved, remaining unmodified after several hours.

### Electric polarization measurements

In these experiments, a triangular waveform was applied at a frequency of 1 kHz across the STO, between the 2DEG and a bottom electrode of Ti/Au, and the current $I$ was measured in real time. Integrating the current over time and normalizing by the sample area yields the polarization.

### Magnetotransport

Low-temperature electrical transport measurements were performed on the thinned samples bonded by Al wires in the van der Pauw

configuration using a standard a.c. lock-in technique ($I_{ac}$ = 200 nA, $f_{ac}$ = 77.03 Hz) in a Quantum Design Dynacool cryostat at a temperature of 2 K and magnetic fields between −9 T and 9 T for the Hall resistance study. Before any back-gate voltage data were recorded, the samples were subjected to a so-called forming step[30] at 2 K, where the back-gate voltage were cycled several times (>2) between the gate-voltage extremes of the particular gate-voltage interval to ensure no irreversible changes would occur in the interface system upon application of the back-gate voltage in the actual experiment. Note that this low-temperature forming step was repeated following all occasions the sample was brought above 105 K. Moreover, at each new cool-down, the samples were always cooled with the back-gate electrostatically grounded.

### *R*–*V* loops measured on NiFe/Al/$SrTiO_3$ samples

Extended Data Figure 3 shows *R*–*V* loops measured on the NiFe/Al/STO sample used for spin pumping. The *R*–*V* and $I_C$–*V* loops have rather similar shapes, indicating a similar origin for both hysteresis effects. The observed two-probe resistance variation of ~0.27 Ω in this 0.4 mm × 2.4 mm NiFe(20 nm)/$AlO_x$//STO sample is compatible with the *R*–*V* for an $AlO_x$//STO sample shown in Fig. 4b. The room-temperature sheet resistance of the NiFe(20 nm)/$AlO_x$//STO sample is roughly that of the NiFe layer, and equal to 9 Ω. In Fig. 4, gating results in a change of the 2DEG sheet resistance from about 1.7 kΩ to 23.5 kΩ. In a simple parallel model of the NiFe(20 nm)/$AlO_x$//STO sample (in which current flows in parallel in the NiFe and the 2DEG), gating should thus result in a sheet resistance change of

$$\Delta R = \left(\frac{R_S^{2DEG} R_S^{NiFe}}{R_S^{2DEG} + R_S^{NiFe}}\right)_{VG-} - \left(\frac{R_S^{2DEG} R_S^{NiFe}}{R_S^{2DEG} + R_S^{NiFe}}\right)_{VG+}$$
$$= \frac{23,500 \times 9}{23,500 + 9} - \frac{1,700 \times 9}{1,700 + 9}$$
$$= 0.044\ \Omega$$

corresponding to an expected two-probe resistance change of 0.26 Ω, in excellent agreement with the observed change of 0.27 Ω. VG− and VG+ indicate negative and positive gate voltages, respectively.

The shape of the *P*–*V* and *R*–*V* loops of Fig. 4 is different from that of the $I_C$–*V* and *R*–*V* data of Extended Data Fig. 3. One reason is that the spin-pumping experiments were performed on a Al//STO sample covered with a NiFe layer to perform the spin injection, whereas the resistance versus electric field (*R*–*E*) and polarization versus electric field (*P*–*E*) loops were performed on Al//STO samples without NiFe and thus with a different electrostatic geometry. Additionally, the sample dimensions are also different for the two sets of experiments. In the spin pumping FMR experiments, the STO thickness is 250 µm, and the lateral size is 0.4 mm × 2.4 mm. For the *R*–*E* and *P*–*E* loop experiments, the STO thickness is 200 µm and the lateral size is 5 mm × 5 mm. Finally, the SP-FMR samples are cut from plain samples, which could induce defects modifying the coercivity. We believe the observed discrepancy between loops to arise primarily from these above-mentioned differences.

## Data availability

The data that support the findings of this study are available from the corresponding authors upon reasonable request.


34. Brataas, A., Tserkovnyak, Y., Bauer, G. E. W. & Halperin, B. I. Spin battery operated by ferromagnetic resonance. *Phys. Rev. B* **66**, 060404 (2002).
35. Costache, M. V., Sladkov, M., Watts, S. M., van der Wal, C. H. & van Wees, B. J. Electrical detection of spin pumping due to the precessing magnetization of a single ferromagnet. *Phys. Rev. Lett.* **97**, 216603 (2006).
36. Ando, K. et al. Inverse spin-Hall effect induced by spin pumping in metallic system. *J. Appl. Phys.* **109**, 103913 (2011).



**Acknowledgements** The authors thank M. Cazayous, B. Dkhil, M. Maglione, S. Gambarelli and V. Maurel for useful discussions, as well as C. Carrétéro, E. Jacquet and Y. Gourdel for technical help. This work received support from the ERC Consolidator grant number 615759 "MINT", the ERC Advanced grant number 833973 "FRESCO", the QUANTERA project "QUANTOX", the French Research Agency (ANR) as part of the "Investissement d'Avenir" programme (LABEX NanoSaclay, ref. ANR-10-LABX-0035) through project "AXION" and the Laboratoire d'Excellence LANEF (ANR-10-LABX-51-01) and ANR project OISO (ANR-17-CE24-0026-03). F.T. acknowledges support by research grant VKR023371 (SPINOX) from VILLUM FONDEN.


**Author contributions** J.-P.A., P.N., L.V. and M.B. designed the experiment. J.-P.A., L.V. and M.B. supervised the study. D.C.V., L.M.V.A. and J.B. prepared the samples. P.N. performed the spin–charge conversion experiments with J.-P.A. and L.V. J.B., S.F. and M.B. performed the polarization measurements with the help of V.G. and F.T. F.T. and J.B. performed the transport experiments and analysed them with M.B. and A.B. M.B. and J.-P.A. wrote the paper with inputs from all authors.

**Competing interests** The authors declare no competing interests.


**Additional information**
**Correspondence and requests for materials** should be addressed to M.B. or J.-P.A.
**Peer review information** *Nature* thanks Dmitri E. Nikonov, Sashi Satpathy and the other, anonymous, reviewer(s) for their contribution to the peer review of this work.
**Reprints and permissions information** is available at http://www.nature.com/reprints.

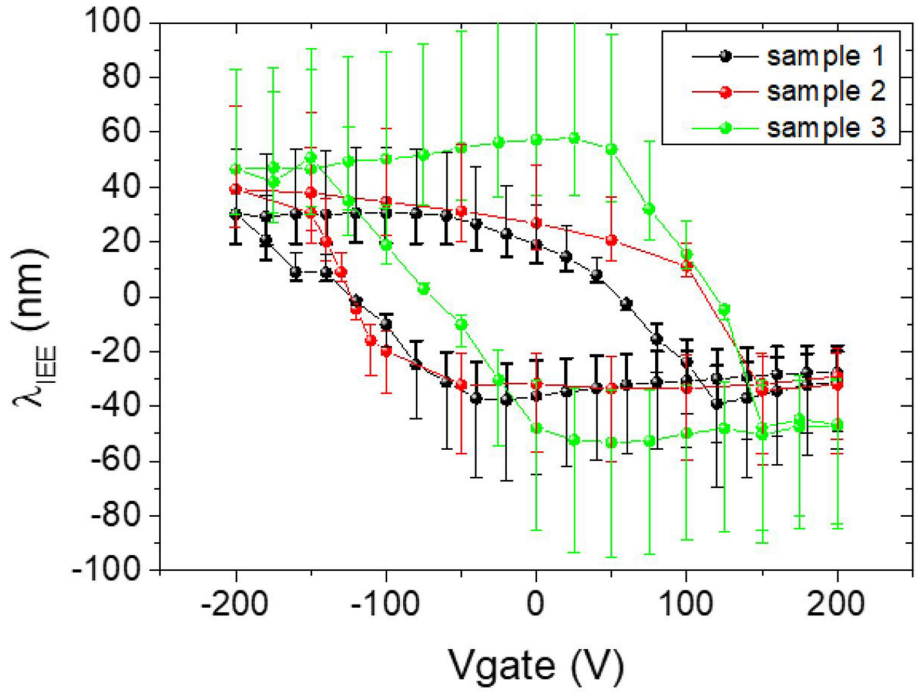


**Extended Data Fig. 1 | Gate-voltage dependence of the inverse Edelstein length in three different samples of NiFe(20 nm)/Al(0.9 nm)//STO.** The error bars are due to the small extra damping measured in this system. The estimated effective spin mixing conductance $G_{eff}^{\uparrow\downarrow}$ is ranging from 1.2 $nm^{-2}$ to 3.2 $nm^{-2}$ with a mean value of 2.2 $nm^{-2}$, leading to an injected spin current $J_S^{3D}$ ranging from 100 to 240 MA $m^{-2}$ $mT^{-2}$, with a mean value of 160 MA $m^{-2}$ $mT^{-2}$.

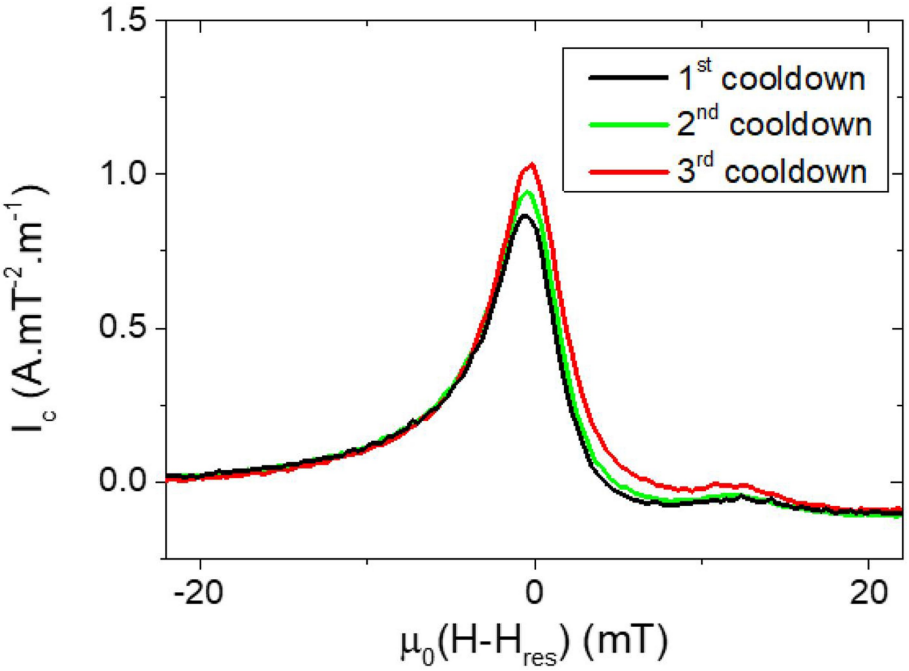


**Extended Data Fig. 2 | Spin-pumping signals obtained at 7 K on sample 2, for three different cool-downs from room temperature.** After each cool-down, the signal was measured before any gate-voltage application.

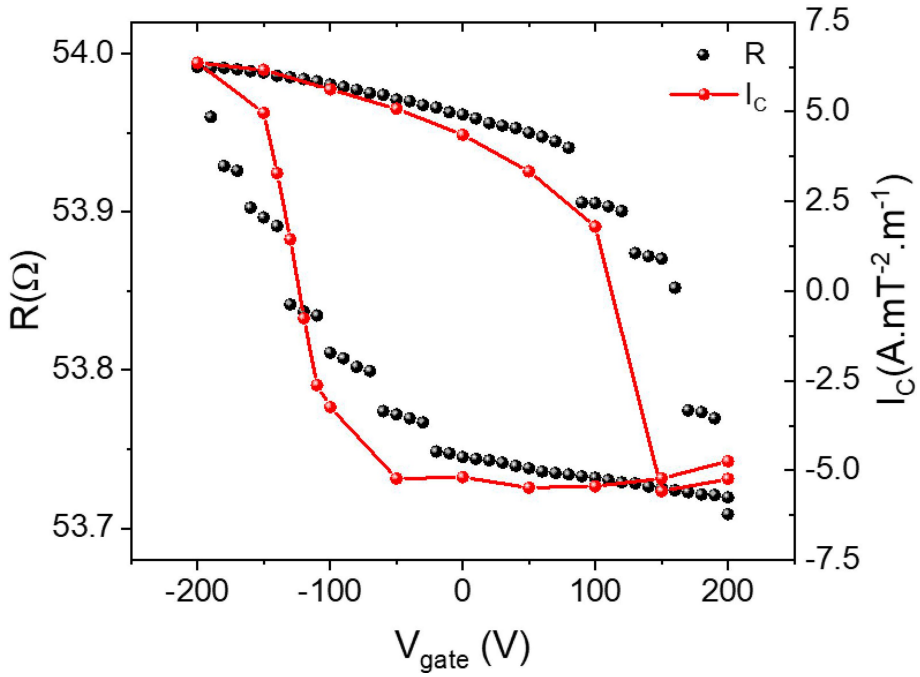


**Extended Data Fig. 3 | Spin-pumping and resistance loops of a NiFe/Al/STO sample.** Black data points, two-probe resistance *R* of a NiFe/Al/STO sample, measured in the spin-pumping setup as a function of the back-gate voltage. Red data points, normalized charge current production ($I_c$) measured by spin pumping.

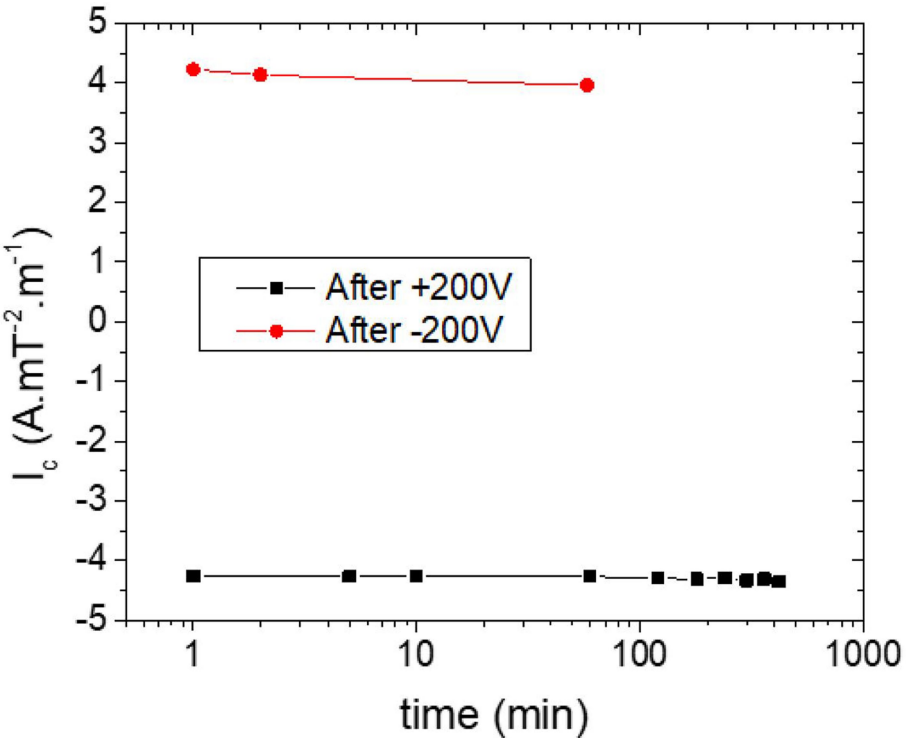


**Extended Data Fig. 4 | Dependence of the produced current on the time spent after application of a positive or negative gate voltage.** Black squares, +200 V; red circles, −200 V. The measurements were performed at 7 K on sample 1.